Biogeosciences Discuss., 10, 14043–14091, 2013
www.biogeosciences-discuss.net/10/14043/2013/
doi:10.5194/bgd-10-14043-2013

Biogeosciences Discussions
Open Access

Spatiotemporal variability and drivers of pCO_2 and air–sea CO_2 fluxes in the California Current System: an eddy-resolving modeling study

G. Turi, Z. Lachkar, and N. Gruber

Environmental Physics, Institute of Biogeochemistry and Pollutant Dynamics, ETH Zürich, Zürich, Switzerland

Received: 7 August 2013 – Accepted: 16 August 2013 – Published: 26 August 2013

Correspondence to: G. Turi (giuliana.turi@env.ethz.ch)

Published by Copernicus Publications on behalf of the European Geosciences Union.

Abstract

We quantify the CO_2 source/sink nature of the California Current System (CalCS) and determine the drivers and processes behind the mean and spatiotemporal variability of the partial pressure of CO_2 (pCO_2) in the surface ocean. To this end, we analyze eddy-resolving, climatological simulations of a coupled physical-ecosystem-biogeochemical ocean model on the basis of the Regional Oceanic Modeling System (ROMS). The model-simulated pCO_2 agrees very well with in situ observations over the entire domain with virtually no bias, but the model overestimates pCO_2 in the nearshore 100 km, and underestimates the observed temporal variability.

In the annual mean, the entire CalCS within 800 km of the coast and from $\sim 33^\circ$ N to 46° N is essentially neutral with regard to atmospheric CO_2. The model simulates an integrated uptake flux of $-0.9\,\mathrm{Tg\,C\,yr^{-1}}$, corresponding to a very small average flux density of $-0.05\,\mathrm{mol\,C\,m^{-2}\,yr^{-1}}$, with an uncertainty of the order of $\pm 0.20\,\mathrm{mol\,C\,m^{-2}\,yr^{-1}}$. This near zero flux is a consequence of an almost complete regional compensation between the strong outgassing in the nearshore region (first 100 km), with flux densities of more than $3\,\mathrm{mol\,C\,m^{-2}\,yr^{-1}}$ and a weaker, but more widespread uptake flux in the offshore region with an average flux density of $-0.17\,\mathrm{mol\,C\,m^{-2}\,yr^{-1}}$. This pattern is primarily a result of the interaction between upwelling in the nearshore that brings waters with high concentrations of dissolved inorganic carbon (DIC) to the surface, and an intense biological drawdown of this DIC, driven by the nutrients that are upwelled together with the DIC. The biological drawdown occurs too slowly to prevent the escape of a substantial amount of CO_2 into the atmosphere, but this is compensated by the biological generation of undersaturated conditions offshore of 100 km, permitting the CalCS to take up most of the escaped CO_2. Thus, the biological pump over the entire CalCS is essentially 100 % efficient, making the preformed DIC and nutrient concentrations of the upwelled waters a primary determinant of the overall source/sink nature of the CalCS. The comparison of the standard simulation with one for preindustrial conditions show that the CalCS is taking up anthropogenic CO_2 at a rate of

BGD
10, 14043–14091, 2013

about $-1\,\mathrm{mol\,C\,m^{-2}\,yr^{-1}}$, implying that the region was a small source of CO_2 to the atmosphere in preindustrial times.

The air–sea CO_2 fluxes vary substantially in time, both on seasonal and sub-seasonal timescales, largely driven by variations in surface ocean pCO_2. There are important differences among the subregions. Notably, the total variance of the fluxes in the central nearshore CalCS is roughly 4–5 times larger than elsewhere. Most of the variability in pCO_2 is associated with the seasonal cycle, except in the nearshore, where sub-seasonal variations driven by mesoscale processes dominate. In the regions offshore of 100 km, changes in surface temperature are the main driver, while in the nearshore region, changes in surface temperature, as well as anomalies in DIC and alkalinity (Alk) owing to changes in circulation, biological productivity and air–sea CO_2 fluxes dominate. The dominance of eddy-driven variability in the nearshore 100 km leads to a complex spatiotemporal mosaic of surface ocean pCO_2 and air–sea CO_2 fluxes that require a substantial observational effort to determine the source/sink nature of this region reliably.

1 Introduction

The coastal ocean often has not been appropriately taken into account in global carbon budget estimates, despite the fact that the associated carbon fluxes are disproportionately large with respect to the small fraction of the global ocean area that coastal oceans occupy (e.g., Liu et al., 2000; Borges et al., 2005; Chavez et al., 2007; Liu et al., 2010; Regnier et al., 2013). Global ocean models tend to be too coarse to resolve important coastal processes and observational data are often limited in space and time (e.g., Laruelle et al., 2010). Therefore, coastal air–sea CO_2 fluxes are currently still relatively poorly quantified, with considerable regional and global uncertainties.

Coastal upwelling regions are particularly dynamic in terms of carbon cycling as they experience extreme temporal and spatial variability in carbon fluxes (e.g., Friederich et al., 2002; Cai et al., 2006; Leinweber et al., 2009; Evans et al., 2011), further adding

BGD
10, 14043–14091, 2013

to the uncertainty in the coastal carbon budget. As the upwelled water is rich in dissolved inorganic carbon (DIC), its partial pressure of CO_2 (pCO_2) is very high and can often exceed atmospheric levels, hence leading to an outgassing of CO_2. At the same time, the upwelled nutrients stimulate phytoplankton productivity, which supports a large fixation and export of organic carbon (e.g., Muller-Karger et al., 2005). This leads to a decrease in surface ocean pCO_2 and enhances the drawdown of atmospheric CO_2 (e.g., Hales et al., 2005, 2012; Chavez and Messié, 2009). These opposing mechanisms and the highly variable ocean circulation with a large amount of mesoscale variability render coastal upwelling systems extremely complex with regard to carbon cycling.

The California Current System (CalCS), one of the four major Eastern Boundary Upwelling Systems (EBUS), exhibits an intricate interplay of physical and biological controls on lateral and air–sea CO_2 fluxes. On the one hand, its relatively high level of eddy activity reduces biological productivity to levels below those expected on the basis of its rate of upwelling, leading also to a reduced vertical export of fixed carbon (Gruber et al., 2011; Lachkar and Gruber, 2011). On the other hand, filaments and other meso- and submesoscale structures cause a substantial lateral export of organic carbon (Nagai et al., 2013), thereby leading to a strong decoupling between biological production and vertical carbon export (Plattner et al., 2005).

The CalCS has been the subject of many studies investigating a variety of different aspects ranging from ecosystem vulnerability to global anthropogenic perturbations such as ocean acidification (e.g., Feely et al., 2008; Gruber et al., 2012; Hauri et al., 2013) and the emergence of areas of hypoxic oxygen concentrations (e.g., Chan et al., 2008), to more process-related topics such as the phenology of coastal upwelling (e.g., Bograd et al., 2009) and the impacts of different processes on biological production (e.g., Gruber et al., 2011; Lachkar and Gruber, 2011, 2013). However, only a few studies have so far dealt with the source/sink nature of the CalCS with regard to atmospheric CO_2 or quantified the contribution of the CalCS to the global carbon budget (Borges et al., 2005; Cai et al., 2006; Chavez et al., 2007; Hales et al., 2012).

BGD
10, 14043–14091, 2013

The published studies have come to rather different conclusions with regard to whether the entire CalCS is a source or a sink of atmospheric CO_2. Using a very limited set of observations, Borges et al. (2005) suggested that the whole Californian coast acts as a weak source with a mean flux density of about 0.5 mol C m^{-2} yr^{-1}. In contrast, Cai et al. (2006) argued that the whole coast between California and Washington acts as a sink with a mean flux density of −1 mol C m^{-2} yr^{-1}, with the Oregon coast having a particularly strong sink strength of −2 mol C m^{-2} yr^{-1}. More recent observations from the Oregon coast support the conclusion of this region being a sink (Hales et al., 2005; Evans et al., 2011), but Evans et al. (2011) also showed that the air–sea CO_2 fluxes in this area are highly variable. In particular, they found very high pCO_2 with values exceeding 1000 µatm in late summer to early fall, while waters in that area were almost consistently undersaturated with respect to the atmosphere in winter and spring. This led to a small annual uptake with a mean flux density of -0.3 ± 6.8 mol C m^{-2} yr^{-1}. A similar small uptake flux was reported for the Santa Monica Bay, using a limited duration, but high frequency time series (Leinweber et al., 2009).

In the first attempt to provide a CalCS-wide estimate without relying on the extrapolation of measurements from one site to the entire region, Chavez et al. (2007) collected all available pCO_2 observations from the Lamont–Doherty Earth Observatory (LDEO) database, and inferred an essentially neutral CalCS with an outgassing flux density of 0.03 mol C m^{-2} yr^{-1}. This corresponds to a total loss of 0.5 Tg C yr^{-1} to the atmosphere over the entire US West Coast and extending ~ 300 km offshore (first three $1^\circ \times 1^\circ$ bins). Using a large set of zonal cruises offshore of Monterey Bay, Pennington et al. (2010) confirmed the nearly balanced air–sea CO_2 budget for the central part of the CalCS, but also emphasized the existence of large onshore-offshore gradients in the fluxes.

Most recently, Hales et al. (2012) refined the estimate by Chavez et al. (2007) using the same data but employing a self organizing map approach to extrapolate the observations in time and space. For the same region, i.e., the area of the central North American Pacific continental margin (22–50° N, within 370 km from the coast), they came to a rather different result, i.e., a moderate sink of −14 Tg C yr^{-1} for the period

BGD
10, 14043–14091, 2013

of 1997 to 2005, corresponding to a flux density of $-0.66\,\mathrm{mol\,C\,m^{-2}\,yr^{-1}}$. They confirmed the strong onshore-offshore differences in pCO_2 and CO_2 fluxes pointed out by Pennington et al. (2010), both in terms of the annual mean and the level of variability.

While these previous studies document the direction and magnitude of the air–sea CO_2 fluxes in different locations of the CalCS and reveal their subseasonal to interannual variability, their lack of consistent geographic settings, the absence of sufficiently dense and spatially extended observational coverage and their differing temporal coverage hinders the emergence of a synthetic view of the CalCS acting as a source or a sink of atmospheric CO_2. This provides an opportunity for numerical models to complement the observational studies as they can provide a synoptic and more complete view of the spatiotemporal variability of the air–sea CO_2 fluxes. The models further offer the opportunity to investigate the processes underlying the mean fluxes and their variability in considerably greater depth than currently possible with the in situ data.

Here, we use a series of eddy-resolving simulations from a coupled physical-ecosystem-biogeochemical oceanic model on the basis of the Regional Oceanic Modeling System (ROMS) to quantify (i) the climatological mean air–sea CO_2 fluxes and their drivers, (ii) the spatiotemporal variability of these fluxes, and (iii) the key drivers and processes behind the variability of these fluxes, i.e., the drivers and processes affecting surface ocean pCO_2. Our study shows that although the CalCS as a whole acts on average as a very weak carbon sink with respect to the atmosphere, the air–sea CO_2 fluxes are locally large and highly variable in space and time. Furthermore, the present work highlights the fundamental contrasts in the dynamics of the carbon cycle that exist between the nearshore areas dominated by the effects of upwelling and biological production and the regions further offshore where variations induced by temperature play a more prominent role. Finally, our investigation reveals that mesoscale eddies contribute substantially to surface pCO_2 variability in the nearshore central CalCS, making it challenging to derive a synoptic and representative view of the CO_2 fluxes on the basis of the sparse observations currently available.

BGD
10, 14043–14091, 2013

2 Methods

2.1 Model details

The model used in this study is an eddy-resolving coupled physical-ecosystem-biogeochemical oceanic model of the US West coast based on the ROMS. The model domain covers roughly 2800 km alongshore (30° N–50° N) and 1250 km offshore (Fig. 1), and has a curvilinear, coast-following grid with an average grid spacing of 5 km. The model's vertical grid consists of 32 depth levels with increasing resolution towards the surface and the shallower nearshore regions. The physical model is based on the UCLA-ETH version of ROMS (Marchesiello et al., 2003; Shchepetkin and McWilliams, 2005).

The ecosystem-biogeochemical model is a nitrogen-based Nutrient-Phytoplankton-Zooplankton-Detritus (NPZD) model and includes a single phytoplankton group, implemented to mimic diatom-like behavior. A comprehensive description of the NPZD model can be found in Gruber et al. (2006). We use the same model setup and ecological parameters as Gruber et al. (2011).

An interactive carbon module was additionally implemented in the model and introduces three new state variables: Dissolved inorganic carbon (DIC), alkalinity (Alk) and calcium carbonate ($CaCO_3$) (Gruber et al., 2012; Hauri et al., 2013; Lachkar and Gruber, 2013). All of these state variables are subject to physical transport and mixing, while $CaCO_3$ is furthermore allowed to sink at a constant rate of 20 m day^{-1}. The organic carbon cycle is linked to the organic nitrogen cycle with a fixed stoichiometric C : N ratio of 106 : 16 (Redfield et al., 1963). DIC concentrations are altered by the air–sea CO_2 flux, the precipitation and dissolution of $CaCO_3$ and the net community production, which is defined as net primary production (NPP) minus heterotrophic respiration. The Alk concentration is modified by the formation and removal of nitrate as well as the precipitation and dissolution of $CaCO_3$. The precipitation of $CaCO_3$ is linked to NPP via a constant proportionality factor of 0.03, meaning that for each formed mole

BGD
10, 14043–14091, 2013

of organic carbon, 0.03 mol of $CaCO_3$ are produced. $CaCO_3$ dissolves at a rate of 0.0057 day^{-1} in the water column and 0.002 day^{-1} in the sediments.

We lowered the production ratio for $CaCO_3$ from the value of 0.07 used previously by Gruber et al. (2011) and Hauri et al. (2013) to account for the fact that their resulting $CaCO_3$ to organic carbon export ratio of 0.25 at 100 m depth was substantially larger than expected, while our new value of 0.09 is consistent with the global mean export ratio of about 0.06 to 0.11 (Lee, 2001; Sarmiento et al., 2002; Jin et al., 2006). In addition, we found that lowering the production ratio also yielded model-simulated pCO_2 that compared better to observations.

The surface ocean carbonate chemistry is calculated following the standard OCMIP carbonate chemistry routines[1]. For all our simulations, atmospheric pCO_2 (pCO_2^{air}) oscillates seasonally around a mean value of 370 µatm, which corresponds approximately to the atmospheric concentration in the years 2000/2001, with a seasonal amplitude of pCO_2^{air} of 2.9 µatm, which was taken from the NOAA Marine Boundary Layer Reference[2] for the mean latitude of our domain.

With the partial pressures of CO_2 of atmosphere (pCO_2^{air}) and surface ocean (pCO_2^{sea}), the air–sea CO_2 flux is computed using the standard bulk formula:

$$F_{CO_2} = -K_0 \cdot k_w \cdot \left(pCO_2^{air} - pCO_2^{sea}\right) \quad (1)$$

where K_0 denotes the solubility of CO_2, computed using the temperature- and salinity-dependent formulation of Weiss (1974), and k_w is the CO_2 gas transfer (piston) velocity. The calculation of the piston velocity for steady (short-term) winds assumes a quadratic dependence on the wind speed (Wanninkhof, 1992), using the coefficient for long-term winds. pCO_2^{sea} is calculated using DIC, Alk, temperature (T), salinity (S) and nutrients, employing the first and second dissociation constants of carbonic acid of Millero (1995), with original reference to Mehrbach et al. (1973) and as refitted by Dickson and Millero

[1] http://ocmip5.ipsl.jussieu.fr/OCMIP/phase3/simulations/NOCES/HOWTO-NOCES-3.html

[2] http://www.esrl.noaa.gov/gmd/ccgg/mbl/mbl.html

BGD
10, 14043–14091, 2013

(1987). Our sign convention is that positive values of F_{CO_2} denote an outgassing of CO_2, while negative values indicate an uptake by the surface ocean.

2.2 Initial and boundary conditions

The model was started from rest and run for 12 yr with monthly climatological forcing. As our model simulations require about 5 yr for the spinup, we use model years 6 to 12 for analysis. The initial and boundary conditions for our runs are as described in Hauri et al. (2013) and Lachkar and Gruber (2013). In particular, the DIC and Alk initial and boundary conditions were derived from the Global Ocean Data Analysis Project (GLODAP; Key et al., 2004). A seasonal cycle was added to Alk in the surface ocean, using the regression approach of Lee et al. (2006) and employing surface ocean T and S. Similarly, a seasonal cycle of surface DIC was constructed using the monthly pCO_2 climatology of Takahashi et al. (2006), and monthly surface Alk, T and S. The seasonal cycles of DIC and Alk are then modeled to penetrate into the upper thermocline, assuming that these variations are proportional to the seasonal amplitude of T at the different depths.

We slightly modified the upper ocean lateral boundary conditions of DIC inferred from GLODAP (Lee et al., 2006; Takahashi et al., 2006) in order to improve upon our model-simulated pCO_2, DIC and Alk fields relative to observations (see more on model evaluation in Sect. 3). The modification consisted of adjusting the vertical profile of DIC with an offset starting value of $-8\,\mathrm{mmol\,C\,m^{-3}}$ at the surface, and then tapering off linearly with density to a depth of 350 m, below which the adjustment is zero. We determined the magnitude of this correction from the model-simulated positive DIC bias of about $10\,\mathrm{mmol\,C\,m^{-3}}$ in the first 10 m relative to data collected from a coast-wide survey cruise undertaken from May to June 2007 by Feely et al. (2008). The most likely reason for the bias in our uncorrected boundary conditions is that they were computed from the gridded products of GLODAP and Takahashi et al. (2006), with particularly the former being based on relatively sparse observations in the eastern North Pacific. The magnitude of the correction is small relative to the uncertainties of GLODAP's DIC

BGD
10, 14043–14091, 2013

gridded product, with the gridding error alone exceeding 10 mmol C m^{-3} for the CalCS (Key et al., 2004).

2.3 Drivers and processes

We employ two complementary approaches to quantify and understand the causes of the spatial and temporal variability in surface ocean pCO_2 in Sects. 5 and 6. The first approach focuses on the drivers, i.e., it aims to identify the role of the different state variables, namely DIC, Alk, T and S, in causing variations in pCO_2. The second approach goes one step further by focusing on the actual processes, i.e., the processes that alter the state variables, namely air–sea CO_2 flux, ocean biology, ocean transport and mixing, and the net fluxes of heat and freshwater (FW) at the ocean surface.

To compute the contribution of each driver to the spatial or temporal variability of pCO_2, we use a first-order Taylor expansion to decompose pCO_2 into four individual components representing contributions from changes in DIC, Alk, T and S. We neglect the very small contribution arising from variations in nutrients. Following Lovenduski et al. (2007) and Doney et al. (2009), we separated the DIC and Alk changes into a part driven by FW fluxes and one driven by other processes, and combined the FW flux-induced changes in DIC and Alk with the changes in S to form a FW flux term, thus:

$$\Delta pCO_2 \approx \underbrace{\frac{\partial pCO_2}{\partial DIC^s} \cdot \Delta DIC^s}_{\Delta pCO_2^{DIC,S}} + \underbrace{\frac{\partial pCO_2}{\partial Alk^s} \cdot \Delta Alk^s}_{\Delta pCO_2^{Alk,S}} + \underbrace{\frac{\partial pCO_2}{\partial T} \cdot \Delta T}_{\Delta pCO_2{}^{T}} + \underbrace{\frac{\partial pCO_2}{\partial FW} \cdot \Delta FW}_{\Delta pCO_2^{FW}} \quad (2)$$

where DIC^s and Alk^s are the salinity-normalized concentrations of DIC and Alk (normalized to a salinity of 34.78 PSU), and where the partial derivatives describe the sensitivities of pCO_2 to small changes in DIC, Alk, T and FW (after Sarmiento and Gruber, 2006, p. 329). We determined the partial derivatives by perturbing each driver by a small amount compared to their respective domain means and recalculating pCO_2

BGD
10, 14043–14091, 2013

with these new values. The Δ-terms are the temporal or spatial anomalies from an annual or domain mean, respectively. The spatial anomalies for each model grid cell were computed as the difference between the in situ pCO_2 of each cell and the domain mean pCO_2 (i.e., $\Delta pCO_2 = pCO_2(x) - \langle pCO_2 \rangle$), while the temporal anomalies were computed as the difference between the pCO_2 at each grid cell and its annual mean (i.e., $\Delta pCO_2 = pCO_2(t) - \overline{pCO_2}$).

This first analysis approach identifies the drivers, but only partially identifies the actual processes causing the changes. In order to identify these processes we ran a series of three sensitivity studies where we consecutively removed the contributions of three main processes (Table 1). In addition, we ran a control simulation (CTRL) with no perturbations to be used as a reference. Due to computational resource limitation, we undertook these simulations at a slightly coarser horizontal resolution of 15 km. These sensitivity simulations were set up to identify the contributions of the air–sea CO_2 flux (S1), of biology (S2) and of solubility (S3). The contribution of solubility to pCO_2 is essentially driven by changes in surface ocean T and S. Upon removal of all these processes, the only process left impacting surface ocean pCO_2 is the influence of ocean circulation on the distribution of DIC and Alk. The latter component together with the biological component represent essentially the net effect of ocean biology on the air–sea CO_2 fluxes. This is because ocean biology not only induces a downward flux of organic matter, which is usually referred to as the biological pump (Volk and Hoffert, 1985), but is also responsible for a very large part of the vertical gradients in DIC and Alk, which are then transported to the surface by ocean circulation (Gruber and Sarmiento, 2002; Sarmiento and Gruber, 2006).

We thus separate the model-simulated pCO_2 from the control run (pCO_2^{Control}) into the following four components:

$$\underbrace{pCO_2^{\text{Control}}}_{\text{CTRL}} = \underbrace{pCO_2^{\text{Gas ex.}}}_{\text{CTRL}-\text{S1}} + \underbrace{pCO_2^{\text{Biology}}}_{\text{S1}-\text{S2}} + \underbrace{pCO_2^{\text{Solubility}}}_{\text{S2}-\text{S3}} + \underbrace{pCO_2^{\text{Circulation}}}_{\text{S3}} \quad (3)$$

BGD
10, 14043–14091, 2013

where we implicitly make the assumption that the contributions of the different processes are linearly additive. Given the non-linearities of the ocean carbonate system (Sarmiento and Gruber, 2006), this is strictly speaking not the case. However, our experience with a permutated sequence showed little difference, indicating that these non-linearities are not substantial enough to alter our results.

The sensitivity runs were conducted in the following manner: In the first sensitivity study (S1) we set the air–sea CO_2 flux coefficient in the model to zero, thereby preventing any exchange of CO_2 between the surface ocean and the atmosphere. The difference in pCO_2 between this simulation and the control simulation, i.e., CTRL – S1, is thus the impact of the air–sea CO_2 flux on pCO_2. In the second sensitivity study (S2), we started from S1, but additionally set incoming solar radiation in the model to zero, thereby inhibiting phytoplankton growth and hence eliminating biological production of organic and inorganic carbon. The difference S1 – S2 is then the impact of biological production on pCO_2. In the third sensitivity study (S3) we eliminated the impact of solubility, i.e., of surface ocean T and S, by setting the CO_2 solubility to a constant value. This was achieved by setting T and S within the solubility equations to domain mean values of 15 °C and 33.1 PSU, respectively. The difference S2 – S3 is then the impact of surface ocean T and S on pCO_2. We end up with a simulation S3 whose only remaining mechanism impacting pCO_2 is circulation acting upon the boundary conditions of DIC and Alk, i.e., transporting and mixing these values from the boundaries into the interior of the domain and then also to the surface, where they impact surface ocean pCO_2.

3 Model evaluation

A thorough model evaluation for sea-surface temperature (SST), chlorophyll, mixed layer depth (MLD), density structure and NPP for the CalCS was presented by Gruber et al. (2011) and Lachkar and Gruber (2011). They found that the model reproduces the annual mean and seasonal patterns of chlorophyll and MLD reasonably well, but

BGD
10, 14043–14091, 2013

that the model has a cold bias of roughly 1 °C compared to satellite data. Further, Gruber et al. (2011) found an underestimation of NPP by the model by about 41 % within 1000 km and 30 % within 100 km from the coast and between 34° N and 42° N compared to satellite-based estimates from Kahru et al. (2009).

We extend the evaluation by comparing the model's simulated sea surface pCO_2 to observations from three different in situ data sources: (i) measurements of the fugacity of CO_2 from the Surface Ocean CO_2 Atlas (SOCAT Version 2; Pfeil et al., 2013), which spans the time period from 1970 to 2011 and includes more than 220 000 observations within our model domain; (ii) pCO_2 measurements from the Global Surface pCO_2 (LDEO) database (Takahashi et al., 2013), spanning the period from 1957 to 2013 for our model domain and consisting of roughly 534 000 measurements; and (iii) pCO_2 data collected by the Naval Postgraduate School and the Monterey Bay Research Aquarium Institute (MBARI) along the California Cooperative Fisheries Investigations' (CalCOFI) Line 67 with more than 7000 data points in our domain for the years 1997 through 2001 (Collins et al., 2003). To facilitate the comparison with the model, we first converted all data to pCO_2, then binned them into 0.5° × 0.5° bins and finally normalized them to the year 2000 assuming a mean annual pCO_2 increase rate of 1.5 µatm yr^{-1} as used in Takahashi et al. (2006). We then regridded the binned and normalized data to match our ROMS curvilinear grid. If bins from different databases overlapped, we gave preference to the SOCAT database. For the subsequent analysis, we only used bins with at least two observations taken in two different months within a season for the seasonal analysis and bins with at least 2 observations from opposite seasons (DJF and JJA, MAM and SON) for the annual mean analysis. This eliminated a large number of bins, particularly in the nearshore region in winter and spring and offshore of 100 km, leaving us with a total of 2021 binned and averaged observations of surface ocean pCO_2. We evaluated our model's performance for 9 subdomains separately, namely a nearshore (0–100 km), a near-offshore (100–400 km) and a far-offshore (400–800 km) subdomain (see contour lines in Fig. 1). The choice of these

BGD
10, 14043–14091, 2013

specific subdomains is based on the magnitude and offshore extent of upwelling, as well as the distinct meridional differences in the structure of the CalCS.

Figure 2 highlights that the model has reasonable to good skills in reproducing the observed near- to offshore gradient of pCO_2 for all seasons, and does particularly well in the summer months when it captures the seasonal upwelling signal near the coast (Fig. 2c). The model also captures the north-south gradients and its seasonal progression, particularly in the offshore regions (Fig. 2a, b and d). Furthermore it reproduces the analysis domain-wide mean pCO_2 very well, with an almost negligible negative bias of less than −0.2 µatm.

A more quantitative assessment of the model's successes and challenges in reproducing the observed pCO_2 is offered by the Taylor diagrams in Fig. 3. The annual mean correlations of the spatial pattern range between about 0.5 and 0.8 and are therefore comparable to those achieved for chlorophyll (Gruber et al., 2011; Lachkar and Gruber, 2011). Also the poorer performance of the model with regard to the seasonal cycle is reminiscent of the generally lower seasonal correlations found for all variables, such as SST, mixed layer depth, and chlorophyll. Much better captured than chlorophyll is the spatial variance of surface ocean pCO_2. While the variance of chlorophyll tends to be underestimated everywhere, the model captures it well for pCO_2: normalized standard deviations for all regions range between 0.7 and 2.4 with annual means between 0.6 for the nearshore region (Fig. 3c) and around 1.1 for the offshore regions (Fig. 3a and b). There exist substantial seasonal differences in the degree to which the spatial variance is captured. While the model overestimates the pCO_2 variance in the far-offshore in all seasons and in spring and fall in the more nearshore regions, it tends to underestimate it in summer and winter in the nearshore and near-offshore regions.

Furthermore, the Taylor diagrams in Fig. 3 reveal substantial regional and temporal differences in the magnitude of the bias in the surface ocean pCO_2. The magnitude of over- and underestimation is largest in the nearshore 0–100 km for all seasons with values ranging between −25 µatm for winter and 46 µatm for summer. Between 100–400 km offshore, the bias varies between −24 µatm in winter and 14 µatm in summer.

BGD
10, 14043–14091, 2013

Similarly in the 400–800 km offshore region, the biases range between −11 µatm for winter and spring and 9 µatm for fall. In the annual mean, the model has a pCO_2 bias of 10 µatm in the nearshore subdomain, and biases of −4 µatm and less than 1 µatm in the near- and far-offshore subdomains, respectively.

The comparison of our model to the ungridded pCO_2 data from CalCOFI Line 67 (Fig. 4), provides us with more detailed information about our model's performance in simulating the onshore-offshore gradient. In accordance with our results for the whole domain, the model mean pCO_2 of each season has a positive bias with respect to the mean observed pCO_2 in the first 100 km, where the model overestimates pCO_2 by up to 300 µatm (summer), but on average agrees very well with the data offshore of 100 km. For all four seasons, the maximum value of modeled pCO_2 peaks closer to the coast than the observed pCO_2, i.e., in the first 10–20 km, and decreases with increasing distance to the coast. The observed pCO_2 however reaches a maximum on average between 20–50 km offshore. One potential explanation for this is that in our model forcing the typical nearshore wind speed drop-off is underestimated (Capet et al., 2004), which would favor more intense coastal upwelling and elevate nearshore pCO_2 levels.

To further check the model's performance, particularly in the nearshore, we compared the modeled surface ocean pCO_2 with that predicted by the neural network model of Hales et al. (2012) for the 6 subdomains within 400 km of the coast (Table 2). This confirms that in the annual mean, our model's overestimation of pCO_2 is larger in the nearshore 0–100 km than in the near-offshore 100–400 km, consistent with our analysis domain-wide model evaluation with the SOCAT, LDEO and MBARI pCO_2 data. Over all these 6 subdomains however, the model has a nearly negligible bias of −0.3 µatm compared to data from Hales et al. (2012).

In conclusion, our model has very good skills in modeling the domain-wide mean pCO_2 and captures the observed spatial and temporal variability of pCO_2 well. In particular, our regional model, although benefiting from the additional constraints provided by the lateral boundary conditions, tends to simulate the observed pCO_2 considerably

BGD
10, 14043–14091, 2013

better than any typical global-scale ocean biogeochemistry model, which often have domain-wide biases of several tens of µatm (e.g., Wanninkhof et al., 2013). However, the model consistently overestimates pCO_2 in the nearshore 100 km, which we verified with various independent databases. We believe this overestimation to be mainly due to deficiencies in our forcing: First, due to the relatively coarse resolution of our wind forcing ($\frac{1}{4}^\circ \times \frac{1}{4}^\circ$), the wind speed may be overestimated in the nearshore (Capet et al., 2004). Second, our use of climatological forcing results in a nearly continuous upwelling along the coast, while in reality, periods of intense upwelling are followed by relaxation periods, when ocean biology can reduce surface ocean pCO_2. Errors in our lateral boundary conditions, the model's too low levels of NPP and biases in the nutrient distributions may also help explain the nearshore pCO_2 biases.

4 Sources and sinks for atmospheric CO_2

4.1 Annual mean fluxes

We model the whole CalCS as a nearly balanced system with regard to atmospheric CO_2, annually taking up only about $-0.9\,\mathrm{Tg\,C\,yr^{-1}}$ over the analysis domain (0–800 km and ~ 33° N–46° N). This corresponds to a tiny average uptake flux density of $-0.05\,\mathrm{mol\,C\,m^{-2}\,yr^{-1}}$ (Table 2). However, this near zero flux hides the presence of strong regional sources and sinks (Figs. 1b and 5). The whole northern subdomain acts as a net sink of $-0.46\,\mathrm{mol\,C\,m^{-2}\,yr^{-1}}$ (Fig. 5a), while the central and southern subdomains are on average sources with flux densities of 0.04 and $0.16\,\mathrm{mol\,C\,m^{-2}\,yr^{-1}}$, respectively (Fig. 5b and c). The domain-wide flux density is nearly that associated with the global oceanic uptake of anthropogenic CO_2 from the atmosphere (e.g., Mikaloff Fletcher et al., 2006; Gruber et al., 2009; Wanninkhof et al., 2013), which one can assume to apply also for the CalCS. Thus the small current uptake flux over the entire CalCS can be interpreted to be largely a consequence of the anthropogenic perturbation of atmospheric CO_2, i.e., nearly all driven by anthropogenic CO_2. In the off-

BGD
10, 14043–14091, 2013

shore direction, the nearshore 100 km is the strongest source, losing CO_2 to the atmosphere with a flux density of 0.78 mol C m^{-2} yr^{-1} (Table 2). In contrast, the area between 100–400 km is the most important contributor to the overall sink with a flux density of −0.47 mol C m^{-2} yr^{-1}. Further offshore of 400 km, the surface ocean is nearly neutral in the annual mean, outgassing on average only 0.05 mol C m^{-2} yr^{-1}. Of the individual subdomains, the central nearshore CalCS between Pt. Conception, California, and Cape Blanco, Oregon, is the strongest CO_2 source, with an average flux density of 1.11 mol C m^{-2} yr^{-1}, whereas the central area between 100–400 km is one of the strongest sink areas with −0.53 mol C m^{-2} yr^{-1} (Fig. 5).

We have not undertaken a systematic investigation of the uncertainties associated with our modeled pCO_2 and air–sea CO_2 fluxes. But some of our sensitivity simulations, where we varied either the boundary conditions or some of the model's parameters within their uncertainty may provide an indication of the order of magnitude of this error. Altering the model's DIC boundary conditions by ±10 mmol C m^{-3}, which corresponds to the model's bias in surface DIC which we established by comparing to data from the Feely et al. (2008) cruise, resulted in a domain-wide pCO_2 change of approximately ±5 µatm, with a corresponding air–sea CO_2 flux change of about ±0.2 mol C m^{-2} yr^{-1}. Changing the $CaCO_3$ production ratio from 0.07 to 0.03 and the use of the set of biological parameters of Gruber et al. (2011) instead of those of Gruber et al. (2006) resulted in domain-wide flux changes within the same uncertainty range. Thus, we estimate that the uncertainty associated with our modeled annual mean flux for the whole domain is at least ±0.20 mol C m^{-2} yr^{-1}, corresponding to an integrated flux uncertainty of ±3.6 Tg C yr^{-1}. In the nearshore, our pCO_2 bias of around 10 µatm corresponds roughly to an error in the CO_2 flux of 0.4 mol C m^{-2} yr^{-1}, so that reducing this bias to zero would cause a decrease in our net outgassing in the nearshore 100 km to around 0.4 mol C m^{-2} yr^{-1}.

Including this rough estimate of the modeled flux uncertainty, our domain mean flux density of −0.05 ± 0.20 mol C m^{-2} yr^{-1} agrees best with the results of Chavez et al. (2007), who suggested the whole US West Coast to act as a nearly balanced, small

BGD
10, 14043–14091, 2013

source of 0.03 mol C m^{-2} yr^{-1}. However, the flux densities of the individual subdomains agree more with the findings of Evans et al. (2011), who showed that the Oregon coast (which is to the largest part included in our northern subdomain) acts as an annual net sink of −0.3 mol C m^{-2} yr^{-1}, and with the results of Pennington et al. (2010), who found that the central California region is nearly balanced.

In order to compare our air–sea CO_2 fluxes more directly to the most comprehensive assessment to date by Hales et al. (2012), we average our results over only the first 0–400 km. This yields an average uptake flux density of −0.17 mol C m^{-2} yr^{-1}, which is smaller than their result of −0.66 mol C m^{-2} yr^{-1} over the same region. However, given the sizable errors in the estimate by Hales et al. (2012) as well as ours, the two estimates are actually statistically indistinguishable. They both agree that the CalCS is essentially neutral with regard to atmospheric CO_2 or a small sink at best.

4.2 Processes and seasonal variability

The annual mean flux pattern is entirely driven by the modeled distribution of the surface ocean pCO_2, which exhibits strong regional differences (Fig. 1a and Table 2). Variations in the gas transfer velocity, responding to regional differences in wind speed, and differences in the CO_2 solubility are, in comparison, of secondary importance, as they only tend to modulate the magnitude of air–sea CO_2 fluxes without influencing their sign (Eq. 1). Furthermore, the temporal variations in atmospheric pCO_2 are very small (e.g., Komhyr et al., 1985; Conway et al., 1994).

The high outgassing in the nearshore regions is a result of surface ocean pCO_2 exceeding 500 µatm there in the annual mean, while the sink regions have strongly undersaturated pCO_2 values of 320 µatm and lower. The domain wide average pCO_2 is very close to that of the atmospheric CO_2, as expected given the near-zero net air–sea CO_2 flux.

The strongest outgassing occurs in summer (during the upwelling season) in the nearshore central CalCS (Fig. 5b), while further offshore in summer outgassing is sub-

BGD
10, 14043–14091, 2013

stantially reduced and there is even an uptake in fall. This pattern is also simulated in the northern area, but to a lesser degree (Fig. 5a). Nearly the whole analysis domain acts as a sink for CO_2 in winter and spring, except for the central and southern nearshore domains, which are sources from spring until fall (Fig. 5b and c). All of the subdomains experience a sign change in CO_2 fluxes during the course of a year, which is consistent with the findings of Hales et al. (2012). This demonstrates that while the net CO_2 flux over the entire CalCS is relatively small, the fluxes vary strongly in space and time, in accordance with findings from previous studies (e.g., Hales et al., 2005, 2012; Chavez et al., 2007; Evans et al., 2011).

We next investigate the drivers and mechanisms for this spatiotemporal variability in more quantitative terms, focusing on the contribution of surface ocean pCO_2 only. This is justified given it being the primary parameter driving the variations in the air–sea CO_2 fluxes. We first quantify the drivers and processes causing the spatial variations, and then investigate the temporal variations on both seasonal and sub-seasonal imescales.

5 Spatial variability of annual mean pCO_2

To highlight the spatial variability of the annual mean surface ocean pCO_2, we subtract its domain average and consider spatial anomalies only (Fig. 6a). Two distinct features can be identified on this plot, which is very close to that of the air–sea pCO_2 difference, given that the domain average pCO_2 differs little from atmospheric pCO_2: (i) large positive anomalies are found in the upwelling area along the coast of the central CalCS, and (ii) there is a division around 38° N between the northern part of the model domain, which tends to have negative anomalies, and the southern part with positive anomalies.

The analysis of the drivers behind this pattern reveals that it is largely a result of strong spatial gradients in DIC^s and T (Fig. 6b and d), with Alk^s having a smaller role and FW fluxes being unimportant (Fig. 6c and e). The strong north-south gradients induced by DIC^s and T tend to cancel each other substantially, so that the largely unopposed onshore-offshore gradient of DIC^s becomes a prominent feature of the annual

BGD
10, 14043–14091, 2013

mean distribution of pCO_2. An exception to this general pattern is the Southern California Bight, where the contribution of Alk^s is important, tending to oppose the effect of DIC^s.

The identification of the processes underlying the spatial pattern in pCO_2 permits us to better understand the processes behind the gradients, and particularly those of the key driver DIC^s (Fig. 7). This process-based separation reveals that the most important contributions to the spatial gradients of annual mean pCO_2 are circulation and biological production (Fig. 7a and b), both of which act upon DIC and Alk. Circulation, i.e., the transport of high DIC and Alk from the boundaries into the domain's interior and then to the surface, leads to high surface ocean pCO_2 values far exceeding atmospheric pCO_2 over most of the domain (Fig. 7a). The high DIC in the upwelled waters push surface pCO_2 up to values around 700 µatm in the upwelling area and between 400–600 µatm further offshore. In the central domain, high pCO_2 values extend particularly far offshore: Values of 550 µatm can still be found around 400–500 km offshore. This large offshore extent is caused by the intense offshore Ekman and eddy-driven transport in the central CalCS (Nagai et al., 2013), which is not strongly opposed by the biological removal of DIC. The upwelled waters are also enriched in Alk, which acts to reduce the impact of the upwelling of DIC on surface ocean pCO_2, but this effect is substantially smaller.

The biological fixation of CO_2 and the subsequent transport of the fixed carbon to depth opposes the circulation effect and acts to decrease pCO_2 nearly everywhere by around 160 µatm on average (Fig. 7b). This biologically-induced pCO_2 drawdown is generally largest in the nearshore region. Yet, unlike physical circulation whose effects are largest in the upwelling area of the central CalCS and decrease with increasing distance to the coast, the biologically-driven pCO_2 drawdown is highest between 50 and 100 km offshore in the central CalCS and extends farther offshore than the physical circulation-driven maximum. This results in the biological compensation of circulation effects being much weaker in the first 50 km nearshore region of the central CalCS in comparison to the rest of the domain. The spatial decoupling between the area of

BGD
10, 14043–14091, 2013

maximum upwelling and the region of maximum biological production has been documented in previous studies of the CalCS and was linked to the large upwelling-driven offshore fluxes of nutrients which are not fully utilized in the coastal upwelling zone (Gruber et al., 2011; Lachkar and Gruber, 2011). The combined effects of circulation and biological production, which we will refer to here as the "biological loop", is hence largest in the first 50–100 km, with values of 500–650 µatm (Fig. 7c). Offshore of 100 km the contribution of the biological loop is nearly homogeneous at around 350 µatm, i.e., below atmospheric CO_2.

In contrast to circulation and biology, the contribution by the air–sea CO_2 flux is comparatively small, contributing ±30 µatm (Fig. 7d). This pattern is directly tied to the regions where the CalCS acts as a source or sink for atmospheric CO_2 (see Fig. 1b). The contribution by the processes affecting the solubility of CO_2 is somewhat larger, amounting to spatial gradients in pCO_2 of up to ±50 µatm (Fig. 7e). This contribution very closely resembles that associated with the T driver (compare with Fig. 6d). This is because variations in T dominate the variations in the CO_2 solubility, while the contribution of FW is very small.

In summary, the net effect of circulation and biological productivity, i.e., the contribution of the biological loop, control to a large extent the distribution of pCO_2 with small differences in the spatial pattern between the two opposing tendencies explaining much of the onshore–offshore gradient. This is because these small differences explain the spatial distribution of DIC^s, the most important driver for the spatial distribution of pCO_2. This also explains the very high pCO_2 values found in the 50 km wide coastal strip in the central CalCS as well as the rapid decrease of pCO_2 with increasing distance to the coast in that region (see Fig. 1a). The processes affecting solubility, i.e., primarily surface ocean T, explain most of the north-south gradient in surface ocean pCO_2, since the combined effect of circulation and biology shows nearly no spatial gradient in the offshore regions, and the air–sea CO_2 flux is largely unimportant.

BGD
10, 14043–14091, 2013

As pCO_2 and the air–sea CO_2 fluxes vary not only on a spatial scale but show also high temporal variability, we next investigate the drivers and processes behind the seasonal and non-seasonal components of pCO_2 variability.

6 Temporal pCO_2 variability

Surface ocean pCO_2 in the CalCS varies substantially in time with a temporal variance of more than 2000 µatm^2 in most of the nearshore areas, i.e., a standard deviation of up to ±50 µatm (Fig. 8a). The variance tapers off quite quickly with increasing offshore distance with a typical variance of about 400 to 800 µatm^2 in the far offshore region, i.e., a standard deviation of between ±20 to ±30 µatm. A good part of this variance is driven by the seasonal cycle (Fig. 8b), especially in the offshore region, where it accounts for almost all of the variance. In contrast, in the nearshore areas of the central CalCS as well as in a region extending out to 200–300 km, the non-seasonal contribution is very substantial, and often exceeds that of the seasonal cycle (Fig. 8c).

6.1 Seasonal variability

To investigate the seasonality of surface ocean pCO_2, we subtract the annual mean pCO_2 from the simulated monthly climatology and consider pCO_2 seasonal anomalies and their drivers following the same approach used for studying the spatial pattern. To capture the contrasting features of pCO_2 seasonality between the coastal and open ocean regions, we analyze nearshore-averaged (less than 100 km offshore) and offshore-averaged temporal anomalies separately. In both the nearshore and offshore regions, positive anomalies of pCO_2 prevail during summer and early fall whereas negative anomalies are observed during the winter and in early spring (black lines in Figs. 9 and 10).

The decomposition of the pCO_2 seasonal anomalies into individual contributions associated with changes in DIC^s, Alk^s, T and FW (Fig. 9) shows that the seasonal vari-

BGD
10, 14043–14091, 2013

ability of pCO_2 in the two regions is driven by distinctly different combinations, whose relative contributions to the seasonal cycle are relatively similar to that discussed for the spatial pattern. In the offshore region, the seasonal cycle is to a very large extent caused by the seasonality of T, i.e., by the seasonal cycle of warming and cooling (Fig. 9a). The pCO_2 variations driven by DIC^s tend to have an opposing seasonal cycle, thereby flattening the simulated pCO_2 relative to that purely driven by T. In contrast, the pCO_2 seasonality in the nearshore region is caused by variations in both T and DIC^s – and to a lesser degree variations in Alk^s and in the FW fluxes (Fig. 9b). Here, the DIC^s-driven variations are about 4 months out of phase with those of T, causing primarily a phase shift of the pCO_2 seasonality relative to the purely T-driven seasonal cycle. The seasonal cycle of the Alk^s-driven component is characterized by higher modes, i.e., further modifying the modeled seasonal cycle of pCO_2.

As was the case for the spatial distribution of pCO_2, we can gain further insight into the working of the seasonal cycle of pCO_2 by analyzing the processes causing the seasonal cycle, i.e., to determine the contributions of the air–sea CO_2 flux, ocean biology, solubility, and ocean circulation.

In the offshore domain, the processes controlling the CO_2 solubility contribute most to the seasonal pCO_2 variability (Fig. 10a). In this region, circulation and biology tend to nearly perfectly balance each other, whereas the air–sea CO_2 flux acts to slightly reduce the overall amplitude of the pCO_2 seasonal cycle (Fig. 10b). In contrast, in the nearshore area circulation, i.e., essentially upwelling, is the most important driver of pCO_2 seasonality. Biological production tends to counteract the circulation effect particularly in spring and early summer. Yet, this biological compensation is only partial, especially during winter when biology has little effect on pCO_2. The seasonal variations in CO_2 solubility also play an important role in the nearshore area, but are less prominent than in the offshore region. Finally, similarly to its role in the offshore region, the air–sea CO_2 flux acts throughout the year to dampen the seasonal cycle of pCO_2.

In conclusion, the simulated seasonality of pCO_2 emerges from the degree of compensation between the solubility-driven pCO_2 variations associated with the seasonal

BGD
10, 14043–14091, 2013

cooling and heating of the surface waters and the circulation/biology-driven variations affecting surface ocean DIC^s and hence pCO_2. In the offshore region, the solubility-driven variations clearly dominate, while circulation/biology can only dampen the seasonality somewhat. In the nearshore regions, the circulation/biology-driven variations are of nearly the same amplitude, but out of phase, leading to a complex seasonal cycle in pCO_2. This is somewhat different, yet overall consistent with our findings with regard to the drivers and processes governing the spatial pCO_2 distribution.

6.2 Mesoscale variability

Our model results show that the non-seasonal component is the dominant variability mode in the first 200–300 km of the central CalCS (Fig. 8c), explaining between 20–70 % of the total pCO_2 variability. Most of this is driven by mesoscale variability, which is more intense in the upwelling regions due to stronger baroclinic instabilities. To further investigate the eddy-driven component of our modeled pCO_2 variability, we analyzed the non-seasonal pCO_2 component as a function of time and offshore distance using Hovmöller diagrams (Fig. 11; Hovmöller, 1949): a comparison of the northern and central offshore transects confirms that the activity attributable to mesoscale and non-seasonal processes is much more prominent in the central area (Fig. 11b), which displays year-round strong eddy activity often reaching out up to 200 km offshore, whereas in the north (Fig. 11a) the eddy activity is detectable only on a seasonal timescale, starting in late summer or early fall. In general, for both domains, strong offshore transport occurs most frequently around the middle of the year.

This high variability associated with eddy activity, which is especially pronounced in the nearshore area, leads to relatively short temporal and spatial decorrelation scales, requiring relatively dense sampling in time and space in order to fully capture the true pCO_2 signal. In the open ocean, Jones et al. (2012) showed that pCO_2 can be correlated over distances of several hundred kilometers, but he also pointed out that these scales are much shorter in the coastal ocean, perhaps as short as a few ten kilometers in space and a few days to weeks in time. However, given that our model is forced with

BGD
10, 14043–14091, 2013

monthly climatologies at the surface and at the lateral boundaries, the fraction of non-seasonal variability is likely underestimated in our simulations. This is because neither long-term variability such as interannual or -decadal variability nor very high frequency variability associated with weather systems are included in our forcing. Furthermore, sub-mesoscale processes like filaments and fronts, which cannot be properly resolved at our model resolution, may further decrease the level of non-seasonal variability in pCO_2. We thus refer to a future study for a more detailed assessment of the required sampling density in order to fully capture the true variability of pCO_2 and the associated air–sea CO_2 fluxes.

7 Discussion

Several questions emerge from our finding that the strong sources and sinks within the CalCS sum up to a nearly balanced system overall with regard to atmospheric CO_2. First, does this nearly complete spatial compensation occur by chance, or are there some underlying mechanisms at play? Second, if such underlying mechanisms exist, how might they control the air–sea CO_2 balance under future climate change? Third, what is the contribution of the oceanic uptake of anthropogenic CO_2 to the overall source/sink balance? Fourth, how do the air–sea CO_2 fluxes within the CalCS compare to fluxes elsewhere, and in particular, how do these results fit into the global picture?

Our analysis of the mechanisms underlying the annual mean air–sea CO_2 fluxes reveal that the near complete spatial compensation is a result of ocean productivity very closely compensating for the effect of ocean circulation on the air–sea CO_2 flux. This latter compensation is not fortuitous, as these two processes are fundamentally linked to each other. This is because they represent the two components of the biological loop, i.e., the downward component largely caused by the downward export of organic matter, and the upward component driven by the upward mixing and transport of the DIC- and Alk-rich deeper waters to the surface (Gruber and Sarmiento, 2002; Sarmiento and Gruber, 2006). As the upward component tends to control also the supply of the

BGD
10, 14043–14091, 2013

limiting nutrient to the near surface ocean, and hence also determines to a large degree the magnitude of biological productivity, the upward and downward components of the biological loop are strongly coupled with each other. The degree of nutrient use efficiency, i.e., the degree to which the upward supplied limiting nutrient is biologically taken up and exported downward again, is a good indicator of the strength of this linkage (Sarmiento and Gruber, 2006). In the CalCS, where nitrate tends to be the limiting nutrient (Eppley and Peterson, 1979), the nitrate use efficiency turns out to be very high, as evidenced by the complete consumption of nitrate in the offshore region. This implies also a very high efficiency of the biological pump, and hence a tendency for an overall near complete compensation between the effects of biology and circulation. This does not occur regionally: in the very nearshore, the nutrient use efficiency is relatively low, allowing a part of the upwelled DIC to escape into the atmosphere. However, as these waters "age" while they are being transported further offshore, the biological pump operates so efficiently that all nitrate is fully utilized, creating the conditions for some of the escaped CO_2 to be taken up again by the surface ocean.

However, the efficiency of the biological pump might change in the future under climate change-driven perturbations such as upwelling-favorable wind intensification and increased stratification. For example, Lachkar and Gruber (2013) show that increasing upwelling-favorable winds results in a decrease in the biological pump efficiency, and hence an increase in the CO_2 outgassing. This is because the large increase in outgassing associated with the upwelling intensification outweighs the effects of the concurrent increase in productivity on surface pCO_2.

It is important to recognize that the anthropogenic perturbation of atmospheric CO_2 has perturbed the air–sea CO_2 fluxes in the CalCS. By comparing our simulations to one were we had set atmospheric CO_2 to a preindustrial value of 270 µatm (Gruber et al., 2012; Hauri et al., 2013), we estimate the domain mean uptake flux of anthropogenic CO_2 in the CalCS to be about $-1\,\mathrm{mol\,C\,m^{-2}\,yr^{-1}}$, which is very close to the global mean (e.g., Mikaloff Fletcher et al., 2006; Gruber et al., 2009; Wanninkhof et al.,

BGD
10, 14043–14091, 2013

2013). This implies that the entire CalCS in preindustrial times was a small net source of CO_2 to the atmosphere.

The different processes controlling surface ocean pCO_2 operate in the CalCS in a manner that is similar to how they impact surface ocean pCO_2 on the global scale, as also there the interaction of ocean circulation and biology is a primary determinant of the spatial distribution of the air–sea CO_2 fluxes (e.g., Gruber and Sarmiento, 2002; Toggweiler et al., 2003; Sarmiento and Gruber, 2006; Gruber et al., 2009). Globally, circulation in the absence of biology tends to increase pCO_2 everywhere, with the efficiency of the biological pump ultimately determining how strong the opposing effect of biology ends up being, i.e., whether a particular region becomes a source or a sink with regard to the biological loop. As the CalCS tends to be a region of relatively high nutrient utilization, the compensation between circulation and biology is nearly complete, helping to explain the relatively small net fluxes if integrated over the whole analysis domain. The high degree of nutrient utilization and the implied high efficiency of the biological pump in the CalCS suggests that this region operates more like the temperate to subpolar North Atlantic, where the biologically-induced fluxes are overall small, and very unlike the North Pacific, where a low nutrient utilization leads to a substantial net outgassing of CO_2 associated with the biological loop (Gruber et al., 2009). We expect also the Canary Current System to operate very similarly to the CalCS given the observed complete nutrient utilization there. In contrast, we expect the Humboldt Current System, where nitrate is often not very efficiently used due to iron limitation, to have a strong net outgassing caused by the inefficient biological pump. While we do not expect large differences in the different EBUS with regard to the solubility-driven component, the CalCS and the North Atlantic differ strongly in this respect, as the strong CO_2 uptake in the North Atlantic is largely driven by its strong cooling.

BGD
10, 14043–14091, 2013

8 Summary and outlook

We used a series of eddy-resolving simulations of the CalCS (i) to assess the climatological mean air–sea CO_2 fluxes and their spatiotemporal variability and (ii) to determine the drivers and processes behind the variability of these fluxes and ultimately surface ocean pCO_2.

Our model results demonstrate that the CalCS is essentially balanced in terms of air–sea CO_2 fluxes, with a very small net uptake flux density of $-0.05 \pm 0.20\,\mathrm{mol\,C\,m^{-2}\,yr^{-1}}$. The fluxes vary strongly locally and on a seasonal timescale, with the nearshore 100 km losing a substantial amount of CO_2 to the atmosphere, which is largely compensated by biologically-driven uptake in the regions offshore of 100 km. We interpret this strong spatial compensation to be the result of a nearly 100 % efficient biological pump, as indicated by the complete utilization of the upwelled limiting nutrient, nitrate. The CalCS acts also as a substantial sink for anthropogenic CO_2, taking up approximately $-1\,\mathrm{mol\,C\,m^{-2}\,yr^{-1}}$, implying that the CalCS was a weak source of CO_2 to the atmosphere in preindustrial times.

Nearly all of the variability in air–sea CO_2 fluxes is caused by surface ocean pCO_2, whose seasonal variability dominates over most of the offshore areas, while in the nearshore 100 km most of the variability is determined by subseasonal, mesoscale activity. The variability in the nearshore is mostly associated with circulation and biological production, which affect DIC, Alk and T, while air–sea CO_2 fluxes, solubility and FW fluxes play a minor role. Offshore of 100 km on the other hand, changes in T are the most important drivers of pCO_2 variability.

One of the main caveats of our model study is that we neither include the high frequency forcing associated with weather-related events, nor longer-term interannual variability. We aim to address this issue in a future study by adding such forcing to our model. We also plan to include an analysis of spatial and temporal decorrelation length scales in order to assess the required sampling density for accurately determining the source/sink nature of the CalCS.

BGD
10, 14043–14091, 2013

Although we made through our model-based study substantial progress in determining the source/sink nature of the CalCS and the mechanisms underlying it, it would be highly desirable to verify this with observations. Clearly, the current network is largely inadequate for this purpose, and would have to be substantially strengthened. Furthermore, accurate quantification of the net air–sea CO_2 fluxes in the CalCS is also becoming increasingly important in the context of studies that aim to verify the emissions of anthropogenic CO_2 in California through measurements of atmospheric CO_2. This is because the large and highly variable air–sea CO_2 fluxes leave a substantial imprint on atmospheric CO_2, which has to be well quantified before the emissions can be inferred. Together with the observations, the models need to be further developed and refined, as they permit to put the observations into a spatiotemporal context, and help assess the relevant processes.

Acknowledgements. This research was financially supported by the Swiss Federal Institute of Technology Zürich (ETH Zürich) and through EU FP7 project CARBOCHANGE "Changes in carbon uptake and emissions by oceans in a changing climate" which received funding from the European Commission's Seventh Framework Programme under grant agreement no. 264879. All simulations were performed at the central computing cluster of ETH Zürich, Brutus. We are grateful to the ROMS and NPZD developers in general, and thank in particular M. Münnich, D. Loher and L. Kropuenske-Artman from ETH Zürich for their invaluable help and support, and G.-K. Plattner for some of the initial analyses. We also thank B. Hales for kindly providing us with his pCO_2 data and R. A. Feely for sharing his cruise database with us, which were used for our model evaluation.

References

Bograd, S. J., Schroeder, I., Sarkar, N., Qiu, X., Sydeman, W. J., and Schwing, F. B.: Phenology of coastal upwelling in the California Current, Geophys. Res. Lett., 36, L01602, doi:10.1029/2008GL035933, 2009. 14046

BGD
10, 14043–14091, 2013

Borges, A., Delille, B., and Frankignoulle, M.: Budgeting sinks and sources of CO_2 in the coastal ocean: diversity of ecosystems counts, Geophys. Res. Lett., 32, L14601, doi:10.1029/2005GL023053, 2005. 14045, 14046, 14047

Cai, W.-J., Dai, M., and Wang, Y.: Air–sea exchange of carbon dioxide in ocean margins: a province-based synthesis, Geophys. Res. Lett., 33, L12603, doi:10.1029/2006GL026219, 2006. 14045, 14046, 14047

Capet, X. J., Marchesiello, P., and McWilliams, J. C.: Upwelling response to coastal wind profiles, Geophys. Res. Lett., 31, L13311, doi:10.1029/2004GL020123, 2004. 14057, 14058

Chan, F., Barth, J. A., Lubchenco, J., Kirincich, A., Weeks, H., Peterson, W. T., and Menge, B. A.: Emergence of anoxia in the California Current large marine ecosystem, Science, 319, 920, doi:10.1126/science.1149016, 2008. 14046

Chavez, F. P. and Messié, M.: A comparison of eastern boundary upwelling ecosystems, Prog. Oceanogr., 83, 80–96, doi:10.1016/j.pocean.2009.07.032, 2009. 14046

Chavez, F. P., Takahashi, T., Cai, W.-J., Friederich, G., Hales, B., Wanninkhof, R., and Feely, R. A.: Coastal oceans, in: The First State of the Carbon Cycle Report (SOCCR): the North American Carbon Budget and Implications for the Global Carbon Cycle, a Report by the US Climate Change Science Program and the Subcommittee on Global Change Research, edited by: King, A., Dilling, L., Zimmerman, G., Fairman, D., Houghton, R., Marland, G., Rose, A., and Wilbanks, T., chap. 15, National Oceanic and Atmospheric Administration, National Climatic Data Center, Asheville, 157–166, 2007. 14045, 14046, 14047, 14059, 14061

Collins, C., Pennington, J., Castro, C., Rago, T., and Chavez, F. P.: The California Current system off Monterey, California: physical and biological coupling, Deep-Sea Res. Pt. II, 50, 2389–2404, doi:10.1016/S0967-0645(03)00134-6, 2003. 14055, 14082, 14083

Conway, T. J., Tans, P. P., Waterman, L. S., Thoning, K. W., Kitzis, D. R., Masarie, K. A., and Zhang, N.: Evidence for interannual variability of the carbon cycle from the National Oceanic and Atmospheric Administration/Climate Monitoring and Diagnostics Laboratory Global Air Sampling Network, J. Geophys. Res., 99, 22831–22855, doi:10.1029/94JD01951, 1994. 14060

Dickson, A. G. and Millero, F. J.: A comparison of the equilibrium constants for the dissociation of carbonic acid in seawater media, Deep-Sea Res. Pt. I, 34, 1733–1743, doi:10.1016/0198-0149(87)90021-5, 1987. 14050

BGD
10, 14043–14091, 2013

Doney, S. C., Lima, I., Feely, R. A., Glover, D. M., Lindsay, K., Mahowald, N., Moore, J. K., and Wanninkhof, R.: Mechanisms governing interannual variability in upper-ocean inorganic carbon system and air–sea CO_2 fluxes: physical climate and atmospheric dust, Deep-Sea Res. Pt. II, 56, 640–655, doi:10.1016/j.dsr2.2008.12.006, 2009. 14052

Eppley, R. W. and Peterson, B. J.: Particulate organic matter flux and planktonic new production in the deep ocean, Nature, 282, 677–680, doi:10.1038/282677a0, 1979. 14068

Evans, W., Hales, B., and Strutton, P. G.: Seasonal cycle of surface ocean pCO_2 on the Oregon shelf, J. Geophys. Res., 116, C05012, doi:10.1029/2010JC006625, 2011. 14045, 14047, 14060, 14061

Feely, R. A., Sabine, C. L., Hernandez-Ayon, J. M., Ianson, D., and Hales, B.: Evidence for upwelling of corrosive "acidified" water onto the continental shelf, Science, 320, 1490–1492, doi:10.1126/science.1155676, 2008. 14046, 14051, 14059

Friederich, G., Walz, P., Burczynski, M., and Chavez, F. P.: Inorganic carbon in the central California upwelling system during the 1997–1999 El Niño–La Niña event, Prog. Oceanogr., 54, 185–203, doi:10.1016/S0079-6611(02)00049-6, 2002. 14045

Gruber, N. and Sarmiento, J. L.: Biogeochemical/physical interactions in elemental cycles, in: The Sea: Biological–Physical Interactions in the Oceans, edited by: Robinson, A. R., McCarthy, J. J., and Rothschild, B., vol. 12, John Wiley and Sons, 337–399, 2002. 14053, 14067, 14069

Gruber, N., Frenzel, H., Doney, S. C., Marchesiello, P., McWilliams, J. C., Moisan, J. R., Oram, J. J., Plattner, G.-K., and Stolzenbach, K. D.: Eddy-resolving simulation of plankton ecosystem dynamics in the California Current System, Deep-Sea Res. Pt. I, 53, 1483–1516, doi:10.1016/j.dsr.2006.06.005, 2006. 14049, 14059

Gruber, N., Gloor, M., Mikaloff Fletcher, S. E., Doney, S. C., Dutkiewicz, S., Follows, M. J., Gerber, M., Jacobson, A. R., Joos, F., Lindsay, K., Menemenlis, D., Mouchet, A., Müller, S. A., Sarmiento, J. L., and Takahashi, T.: Oceanic sources, sinks, and transport of atmospheric CO_2, Global Biogeochem. Cy., 23, GB1005, doi:10.1029/2008GB003349, 2009. 14058, 14068, 14069

Gruber, N., Lachkar, Z., Frenzel, H., Marchesiello, P., Münnich, M., McWilliams, J. C., Nagai, T., and Plattner, G.-K.: Eddy-induced reduction of biological production in eastern boundary upwelling systems, Nat. Geosci., 4, 787–792, doi:10.1038/ngeo1273, 2011. 14046, 14049, 14050, 14054, 14055, 14056, 14059, 14063

BGD
10, 14043–14091, 2013

Gruber, N., Hauri, C., Lachkar, Z., Loher, D., Frölicher, T. L., and Plattner, G.-K.: Rapid progression of ocean acidification in the California Current System, Science, 337, 220–223, doi:10.1126/science.1216773, 2012. 14046, 14049, 14068

Hales, B., Takahashi, T., and Bandstra, L.: Atmospheric CO_2 uptake by a coastal upwelling system, Global Biogeochem. Cy., 19, GB1009, doi:10.1029/2004GB002295, 2005. 14046, 14047, 14061

Hales, B., Strutton, P. G., Saraceno, M., Letelier, R., Takahashi, T., Feely, R. A., Sabine, C., and Chavez, F.: Satellite-based prediction of pCO_2 in coastal waters of the eastern North Pacific, Prog. Oceanogr., 103, 1–15, doi:10.1016/j.pocean.2012.03.001, 2012. 14046, 14047, 14057, 14060, 14061, 14080

Hauri, C., Gruber, N., Vogt, M., Doney, S. C., Feely, R. A., Lachkar, Z., Leinweber, A., McDonnell, A. M. P., Munnich, M., and Plattner, G.-K.: Spatiotemporal variability and long-term trends of ocean acidification in the California Current System, Biogeosciences, 10, 193–216, doi:10.5194/bg-10-193-2013, 2013. 14046, 14049, 14050, 14051, 14068

Hovmöller, E.: The Trough-and-Ridge diagram, Tellus, 1, 62–66, doi:10.1111/j.2153-3490.1949.tb01260.x, 1949. 14066, 14091

Jin, X., Gruber, N., Dunne, J. P., Sarmiento, J. L., and Armstrong, R. A.: Diagnosing the contribution of phytoplankton functional groups to the production and export of particulate organic carbon, $CaCO_3$, and opal from global nutrient and alkalinity distributions, Global Biogeochem. Cy., 20, GB2015, doi:10.1029/2005GB002532, 2006. 14050

Jones, S., Le Quéré, C., and Rödenbeck, C.: Autocorrelation characteristics of surface ocean pCO_2 and air–sea CO_2 fluxes, Global Biogeochem. Cy., 26, GB2042, doi:10.1029/2010GB004017, 2012. 14066

Kahru, M., Kudela, R., Manzano-Sarabia, M., and Mitchell, B. G.: Trends in primary production in the California Current detected with satellite data, J. Geophys. Res., 114, C02004, doi:10.1029/2008JC004979, 2009. 14055

Key, R. M., Kozyr, A., Sabine, C. L., Lee, K., Wanninkhof, R., Bullister, J. L., Feely, R. A., Millero, F. J., Mordy, C., and Peng, T.-H.: A global ocean carbon climatology: results from Global Data Analysis Project (GLODAP), Global Biogeochem. Cy., 18, GB4031, doi:10.1029/2004GB002247, 2004. 14051, 14052

Komhyr, W., Gammon, R., Harris, T., Waterman, L. S., Conway, T., Taylor, W., and Thoning, K.: Global atmospheric distribution and variations from 1968–1982 NOAA/GMCC CO_2

BGD
10, 14043–14091, 2013

flask sample data, J. Geophys. Res., 90, 5567–5596, doi:10.1029/JD090iD03p05567, 1985. 14060

Lachkar, Z. and Gruber, N.: What controls biological production in coastal upwelling systems? Insights from a comparative modeling study, Biogeosciences, 8, 2961–2976, doi:10.5194/bg-8-2961-2011, 2011. 14046, 14054, 14056, 14063

Lachkar, Z. and Gruber, N.: Response of biological production and air–sea CO_2 fluxes to upwelling intensification in the California and Canary Current Systems, J. Marine Syst., 109–110, 149–160, doi:10.1016/j.jmarsys.2012.04.003, 2013. 14046, 14049, 14051, 14068

Laruelle, G. G., Dürr, H. H., Slomp, C. P., and Borges, A. V.: Evaluation of sinks and sources of CO_2 in the global coastal ocean using a spatially-explicit typology of estuaries and continental shelves, Geophys. Res. Lett., 37, L15607, doi:10.1029/2010GL043691, 2010. 14045

Lee, K.: Global net community production estimated from the annual cycle of surface water total dissolved inorganic carbon, Limnol. Oceanogr., 46, 1287–1297, doi:10.4319/lo.2001.46.6.1287, 2001. 14050

Lee, K., Tong, L. T., Millero, F. J., Sabine, C. L., Dickson, A. G., Goyet, C., Park, G.-H., Wanninkhof, R., Feely, R. A., and Key, R. M.: Global relationships of total alkalinity with salinity and temperature in surface waters of the world's oceans, Geophys. Res. Lett., 33, L19605, doi:10.1029/2006GL027207, 2006. 14051

Leinweber, A., Gruber, N., Frenzel, H., Friederich, G., and Chavez, F. P.: Diurnal carbon cycling in the surface ocean and lower atmosphere of Santa Monica Bay, California, Geophys. Res. Lett., 36, L08601, doi:10.1029/2008GL037018, 2009. 14045, 14047

Liu, K.-K., Atkinson, L., Chen, C. A., Gao, S., Hall, J., MacDonald, R., Talaue-McManus, L., and Quiñones, R.: Exploring continental margin carbon fluxes on a global scale, EOS T. Am. Geophys. Un., 81, 641–644, doi:10.1007/978-3-540-92735-8, 2000. 14045

Liu, K.-K., Atkinson, L., Quiñones, R., and Talaue-McManus, L.: Biogeochemistry of continental margins in a global context, in: Carbon and Nutrient Fluxes in Continental Margins, Global Change – The IGBP Series, edited by: Liu, K.-K., Atkinson, L., Quiñones, R., and Talaue-McManus, L., Springer, Berlin, Heidelberg, 3–24, doi:10.1007/978-3-540-92735-8, 2010. 14045

Lovenduski, N. S., Gruber, N., Doney, S. C., and Lima, I. D.: Enhanced CO_2 outgassing in the Southern Ocean from a positive phase of the Southern Annular Mode, Global Biogeochem. Cy., 21, GB2026, doi:10.1029/2006GB002900, 2007. 14052

BGD
10, 14043–14091, 2013

Marchesiello, P., McWilliams, J. C., and Shchepetkin, A.: Equilibrium structure and dynamics of the California Current System, J. Phys. Oceanogr., 33, 753–783, doi:10.1175/1520-0485(2003)33<753:ESADOT>2.0.CO;2, 2003. 14049

Mehrbach, C., Culberson, C., Hawley, J., and Pytkowicz, R.: Measurement of the apparent dissociation constants of carbonic acid in seawater at atmospheric pressure, Limnol. Oceanogr., 18, 897–907, doi:10.4319/lo.1973.18.6.0897, 1973. 14050

Mikaloff Fletcher, S. E., Gruber, N., Jacobson, A. R., Doney, S. C., Dutkiewicz, S., Gerber, M., Follows, M., Joos, F., Lindsay, K., Menemenlis, D., Mouchet, A., Müller, S. A., and Sarmiento, J. L.: Inverse estimates of anthropogenic CO_2 uptake, transport, and storage by the ocean, Global Biogeochem. Cy., 20, GB2002, doi:10.1029/2005GB002530, 2006. 14058, 14068

Millero, F. J.: Thermodynamics of the carbon dioxide system in the oceans, Geochim. Cosmochim. Ac., 59, 661–677, doi:10.1016/0016-7037(94)00354-O, 1995. 14050

Muller-Karger, F. E., Varela, R., Thunell, R., Luerssen, R., Hu, C., and Walsh, J. J.: The importance of continental margins in the global carbon cycle, Geophys. Res. Lett., 32, L01602, doi:10.1029/2004GL021346, 2005. 14046

Nagai, T., Gruber, N., Frenzel, H., McWilliams, J. C., and Plattner, G.-K.: Dominant role of eddies in offshore transport in the California Current System, in prep., 2013. 14046, 14062

Pennington, J., Castro, C., Collins, C., Evans, W., Friederich, G., Michisaki, R., and Chavez, F.: The Northern and Central California Coastal Upwelling System, in: Carbon and Nutrient Fluxes in Continental Margins, Global Change – The IGBP Series, edited by: Liu, K.-K., Atkinson, L., Quiñones, R., and Talaue-McManus, L., Springer, Berlin, Heidelberg, 29–44, 2010. 14047, 14048, 14060

Pfeil, B., Olsen, A., Bakker, D. C. E., Hankin, S., Koyuk, H., Kozyr, A., Malczyk, J., Manke, A., Metzl, N., Sabine, C. L., Akl, J., Alin, S. R., Bates, N., Bellerby, R. G. J., Borges, A., Boutin, J., Brown, P. J., Cai, W.-J., Chavez, F. P., Chen, A., Cosca, C., Fassbender, A. J., Feely, R. A., González-Dávila, M., Goyet, C., Hales, B., Hardman-Mountford, N., Heinze, C., Hood, M., Hoppema, M., Hunt, C. W., Hydes, D., Ishii, M., Johannessen, T., Jones, S. D., Key, R. M., Körtzinger, A., Landschützer, P., Lauvset, S. K., Lefèvre, N., Lenton, A., Lourantou, A., Merlivat, L., Midorikawa, T., Mintrop, L., Miyazaki, C., Murata, A., Nakadate, A., Nakano, Y., Nakaoka, S., Nojiri, Y., Omar, A. M., Padin, X. A., Park, G.-H., Paterson, K., Perez, F. F., Pierrot, D., Poisson, A., Ríos, A. F., Santana-Casiano, J. M., Salisbury, J., Sarma, V. V. S. S., Schlitzer, R., Schneider, B., Schuster, U., Sieger, R., Skjelvan, I., Steinhoff, T., Suzuki, T.,

BGD
10, 14043–14091, 2013

Takahashi, T., Tedesco, K., Telszewski, M., Thomas, H., Tilbrook, B., Tjiputra, J., Vandemark, D., Veness, T., Wanninkhof, R., Watson, A. J., Weiss, R., Wong, C. S., and Yoshikawa-Inoue, H.: A uniform, quality controlled Surface Ocean CO_2 Atlas (SOCAT), Earth Syst. Sci. Data, 5, 125–143, doi:10.5194/essd-5-125-2013, 2013. 14055, 14082, 14083

Plattner, G.-K., Gruber, N., Frenzel, H., and McWilliams, J. C.: Decoupling marine export production from new production, Geophys. Res. Lett., 32, L11612, doi:10.1029/2005GL022660, 2005. 14046

Redfield, A., Ketchum, B., and Richards, F.: The influence of organisms on the composition of seawater, in: The Sea: Ideas and Observations on Progress in the Study of the Sea, edited by: Hill, M., Wiley Interscience, New York, 26–77, 1963. 14049

Regnier, P., Friedlingstein, P., Ciais, P., Mackenzie, F. T., Gruber, N., Janssens, I. A., Laruelle, G. G., Lauerwald, R., Luyssaert, S., Andersson, A. J., Arndt, S., Arnosti, C., Borges, A. V., Dale, A. W., Gallego-Sala, A., Goddéris, Y., Goossens, N., Hartmann, J., Heinze, C., Ilyina, T., Joos, F., LaRowe, D. E., Leifeld, J., Meysman, F. J. R., Munhoven, G., Raymond, P. A., Spahni, R., Suntharalingam, P., and Thullner, M.: Anthropogenic perturbation of the carbon fluxes from land to ocean, Nat. Geosci., 6, 597–607, doi:10.1038/ngeo1830, 2013. 14045

Sarmiento, J. L. and Gruber, N.: Ocean Biogeochemical Dynamics, Princeton University Press, Princeton, New Jersey, 2006. 14052, 14053, 14054, 14067, 14068, 14069

Sarmiento, J. L., Dunne, J., Gnanadesikan, A., Key, R. M., Matsumoto, K., and Slater, R.: A new estimate of the $CaCO_3$ to organic carbon export ratio, Global Biogeochem. Cy., 16, 1107, doi:10.1029/2002GB001919, 2002. 14050

Shchepetkin, A. F. and McWilliams, J. C.: The regional oceanic modeling system (ROMS): a split-explicit, free-surface, topography-following-coordinate oceanic model, Ocean Model., 9, 347–404, doi:10.1016/j.ocemod.2004.08.002, 2005. 14049

Takahashi, T., Sutherland, S. C., Feely, R. A., and Wanninkhof, R.: Decadal change of the surface water pCO_2 in the North Pacific: a synthesis of 35 years of observations, J. Geophys. Res., 111, C07S05, doi:10.1029/2005JC003074, 2006. 14051, 14055

Takahashi, T., Sutherland, S., and Kozyr, A.: Global ocean surface water partial pressure of CO_2 database: Measurements performed during 1957–2012 (Version 2012). ORNL/CDIAC-160, NDP-088(V2012), Carbon Dioxide Information Analysis Center, Oak Ridge National Laboratory, US Department of Energy, Oak Ridge, Tennessee, doi:10.3334/CDIAC/OTG.NDP088(V2012), 2013. 14055, 14082, 14083

BGD
10, 14043–14091, 2013

Taylor, K. E.: Summarizing multiple aspects of model performance in a single diagram, J. Geophys. Res., 106, 7183–7192, doi:10.1029/2000JD900719, 2001. 14083
Toggweiler, J. R., Murnane, R., Carson, S., Gnanadesikan, A., and Sarmiento, J. L.: Representation of the carbon cycle in box models and GCMs, 2. Organic pump, Global Biogeochem. Cy., 17, 1027, doi:10.1029/2001GB001841, 2003. 14069
Volk, T. and Hoffert, M. I.: Ocean carbon pumps: Analysis of relative strengths and efficiencies in ocean-driven atmospheric CO_2 changes, in: The Carbon Cycle and Atmospheric CO_2: Natural Variations Archean to Present, Geophysical Monograph Series, edited by: Sundquist, E. T. and Broecker, W. S., vol. 32, Washington, D.C., 99–110, doi:10.1029/GM032p0099, 1985. 14053
Wanninkhof, R.: Relationship between wind speed and gas exchange over the ocean, J. Geophys. Res., 97, 7373–7382, doi:10.1029/92JC00188, 1992. 14050
Wanninkhof, R., Park, G. -H., Takahashi, T., Sweeney, C., Feely, R., Nojiri, Y., Gruber, N., Doney, S. C., McKinley, G. A., Lenton, A., Le Quéré, C., Heinze, C., Schwinger, J., Graven, H., and Khatiwala, S.: Global ocean carbon uptake: magnitude, variability and trends, Biogeosciences, 10, 1983–2000, doi:10.5194/bg-10-1983-2013, 2013. 14058, 14068
Weiss, R. F.: Carbon dioxide in water and seawater: the solubility of a non-ideal gas, Mar. Chem., 2, 203–215, doi:10.1016/0304-4203(74)90015-2, 1974. 14050

BGD
10, 14043–14091, 2013

Table 1. Calculation of the contributions of air–sea CO_2 flux, biological production, CO_2 solubility and circulation to the total pCO_2 from the control simulation.

Simulation	Properties
CTRL	Control simulation
S1	No air–sea CO_2 flux
S2	No air–sea CO_2 flux, no biological production
S3	No air–sea CO_2 flux, no biological production, constant CO_2 solubility
Calculation	**Implication**
CTRL – S1	Contribution of air–sea CO_2 flux to total pCO_2
S1 – S2	Contribution of biological production to total pCO_2
S2 – S3	Contribution of CO_2 solubility to total pCO_2
S3	"Pure circulation": pCO_2 if only circulation existed

BGD
10, 14043–14091, 2013

Table 2. Regional variability of surface pCO_2 and air–sea CO_2 fluxes in the CalCS. ΔpCO_2 is $pCO_2^{sea} - pCO_2^{air}$ (370 µatm) and Hales et al. (2012) pCO_2 bias refers to pCO_2 from our study minus pCO_2 from Hales et al. (2012).

Domain	Surface area	ΔpCO_2	Hales et al. (2012) pCO_2 bias	Air–sea CO_2 flux density	Integrated air–sea CO_2 flux
Units	km^2	µatm	µatm	$mol\,C\,m^{-2}\,yr^{-1}$	$Tg\,C\,yr^{-1}$
Nearshore					
north	33 781	−19.0	33.6	0.01	<0.01
central	112 973	15.7	3.3	1.11	1.5
south	21 681	6.7	25.4	0.26	0.1
total	168 435	7.2	11.6	0.78	1.6
Near-offshore					
north	108 403	−32.3	3.2	−0.49	−0.6
central	351 808	−20.9	−8.4	−0.53	−2.2
south	65 365	−3.9	4.9	−0.15	−0.1
total	525 576	−21.1	−4.3	−0.47	−3.0
Far-offshore					
north	174 720	−17.7	n/a	−0.53	−1.1
central	531 430	4.6	n/a	0.19	1.2
south	92 230	11.1	n/a	0.36	0.4
total	798 380	0.8	n/a	0.05	0.5
CalCS total	1 492 391	−6.6	n/a	-0.05 ± 0.20	-0.9 ± 3.6

BGD
10, 14043–14091, 2013

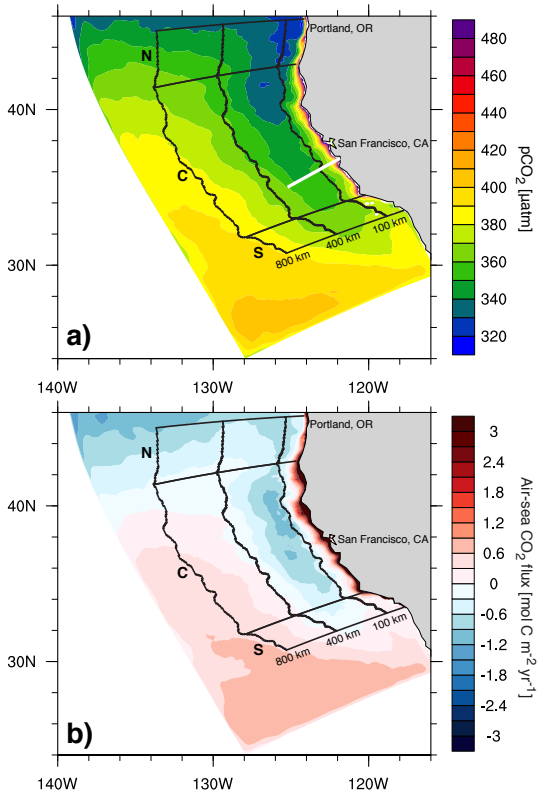

Fig. 1. Annual mean surface pCO_2 **(a)** and air–sea CO_2 flux **(b)** as simulated in the CalCS. Positive air–sea fluxes denote an outgassing of CO_2. The superimposed black lines indicate the nine subdomains, where the northern (N), central (C) and southern (S) subdomains are all split into a nearshore (0–100 km), a near-offshore (100–400 km) and a far-offshore (400–800 km) subdomain. The white line in panel **(a)** indicates the approximate location of the MBARI/CalCOFI Line 67.

BGD
10, 14043–14091, 2013

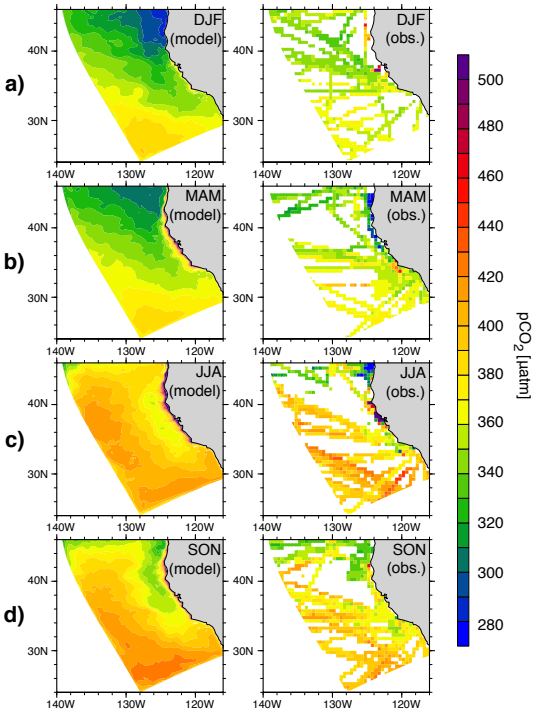

Fig. 2. Seasonally averaged modeled (left column) and observed (right column) surface pCO_2 for winter (**a**; DJF), spring (**b**; MAM), summer (**c**; JJA) and fall (**d**; SON). Observations are pCO_2 computed from the Surface Ocean CO_2 Atlas (SOCAT Version 2; Pfeil et al., 2013), the Global Surface pCO_2 database (Takahashi et al., 2013) and the MBARI/CalCOFI Line 67 (Collins et al., 2003). The data were first binned to $0.5^\circ \times 0.5^\circ$ bins to compute a climatology, normalized to the year 2000 and then regridded to match the ROMS grid. The right column shows all the bins, independent of the number of observations in them.

BGD
10, 14043–14091, 2013

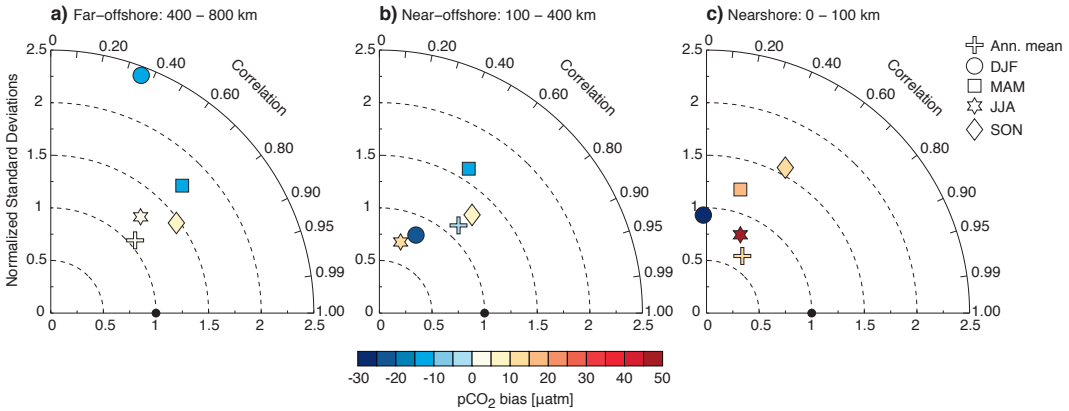

Fig. 3. Taylor diagram (Taylor, 2001) of modeled vs. observed pCO_2 for the far-offshore **(a)**, near-offshore **(b)** and nearshore **(c)** subdomains. Observations are from the Surface Ocean CO_2 Atlas (SOCAT Version 2; Pfeil et al., 2013), the Global Surface pCO_2 database (Takahashi et al., 2013) and the MBARI/CalCOFI Line 67 (Collins et al., 2003). The distance to the origin point (dashed lines) indicates the modeled field's standard deviations, normalized to the standard deviation of observations (i.e., a value of 1 would mean a perfect agreement with the observed spatial variability). The Spearman correlation coefficient for the model vs. the observations is represented by the angle between the model point and vertical axis. The distance from the observation reference point (black dot) to the model point indicates that model field's central pattern root mean square. The color code indicates the bias of the modeled vs. the observed pCO_2: positive values mean the model overestimates pCO_2 and vice versa.

BGD
10, 14043–14091, 2013

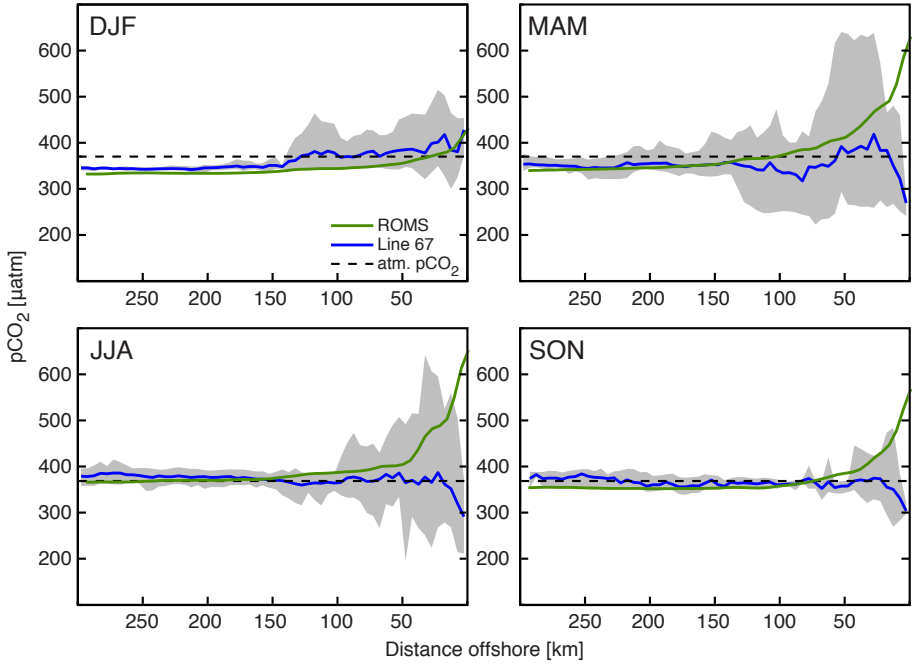

Fig. 4. Seasonally averaged pCO_2 from our model (green line) and from MBARI/CalCOFI Line 67 (blue line) as a function of distance offshore. The gray shaded area represents the range of observed pCO_2 within each season. The dashed black line indicates our model's annual mean atmospheric pCO_2 of 370 µatm.

BGD
10, 14043–14091, 2013

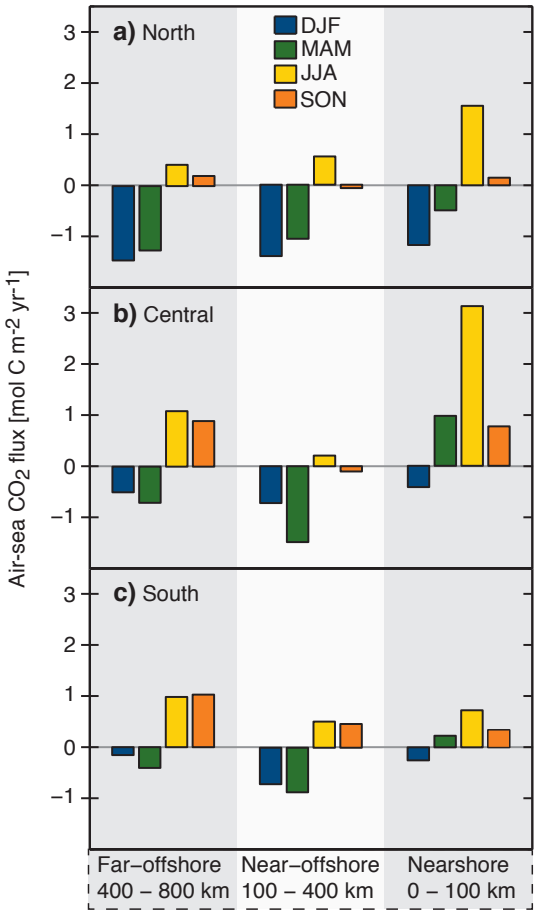

Fig. 5. Seasonally averaged air–sea CO_2 flux for the northern **(a)**, central **(b)** and southern **(c)** subdomains in the nearshore, near-offshore and far-offshore. Positive values denote an outgassing of CO_2, negative values an uptake by the surface ocean.

BGD
10, 14043–14091, 2013

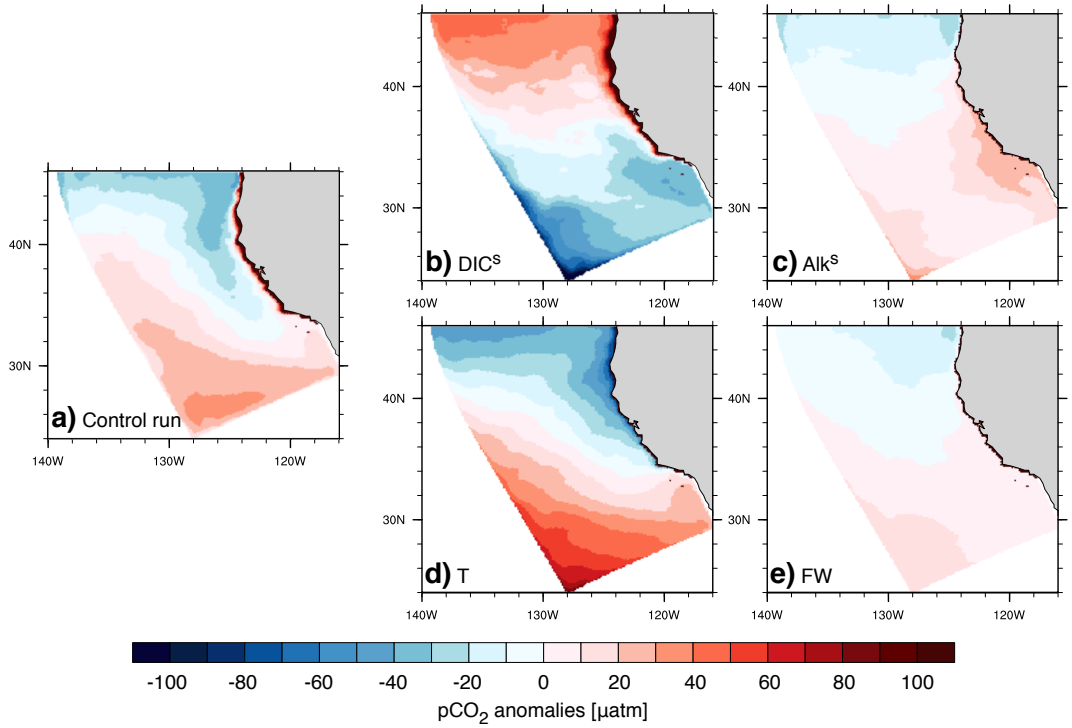

Fig. 6. Spatial pCO_2 anomalies computed as the difference between in situ and domain mean pCO_2. Panel **(a)** shows total pCO_2 anomalies in the control simulation and panels **(b–e)** show the contributions of the four drivers DIC^s, Alk^s, T and FW to the total.

BGD
10, 14043–14091, 2013

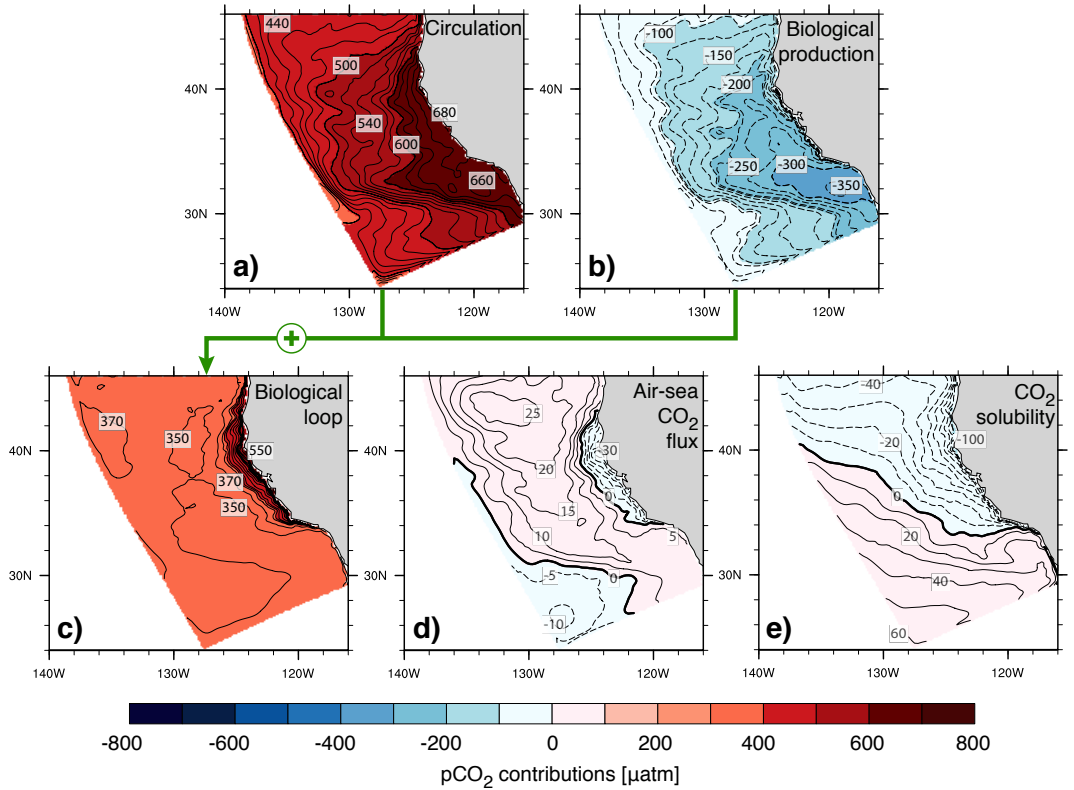

Fig. 7. Contributions of ocean circulation **(a)**, biological production **(b)**, air–sea CO_2 flux **(d)** and CO_2 solubility **(e)** to annual mean pCO_2 as simulated in the control simulation. Panel **(c)** represents the contribution of the biological loop, i.e., the sum of **(a)** and **(b)** (indicated by the green line). Positive contributions are displayed as solid lines, negative contributions as dashed lines.

BGD
10, 14043–14091, 2013

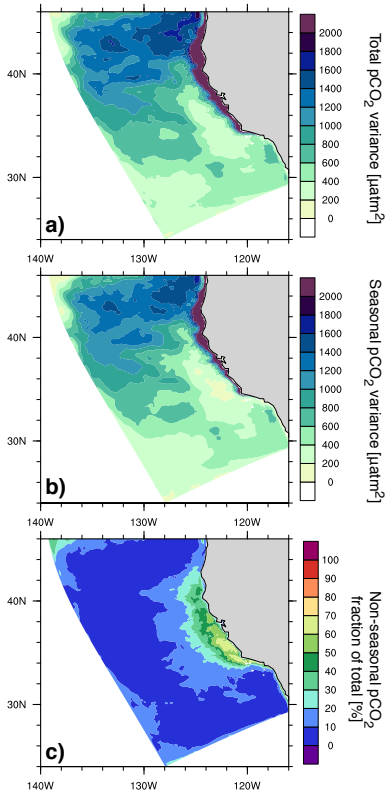

Fig. 8. Total pCO_2 variance **(a)** computed from 2-day output spanning seven consecutive model years, and seasonal pCO_2 variance **(b)** derived from a fitted mean over the same seven years. Panel **(c)** shows the fraction of the total pCO_2 attributable to non-seasonal variability.

BGD
10, 14043–14091, 2013

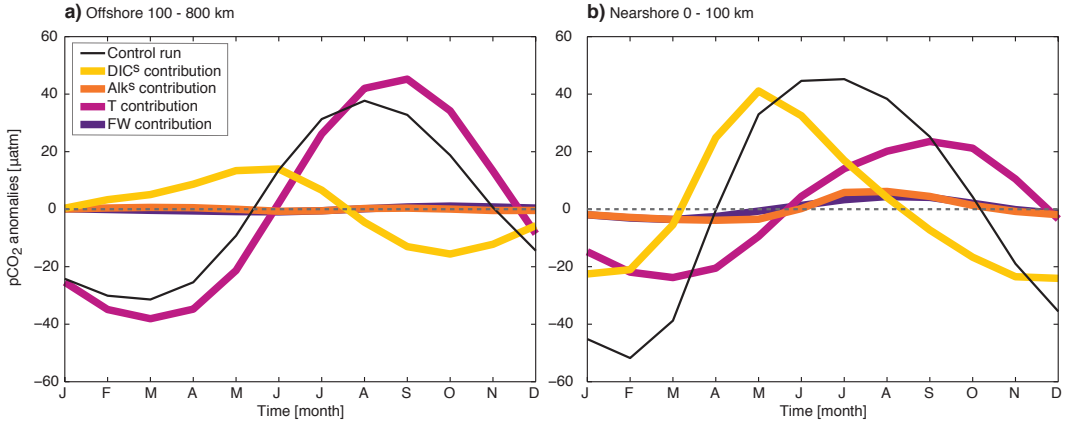

Fig. 9. Monthly mean pCO_2 anomalies for the offshore **(a)** and the nearshore **(b)** domains: the colored lines represent the contributions of the four drivers DIC^s, Alk^s, T and FW to monthly mean pCO_2 anomalies from the control simulation (black line).

BGD
10, 14043–14091, 2013

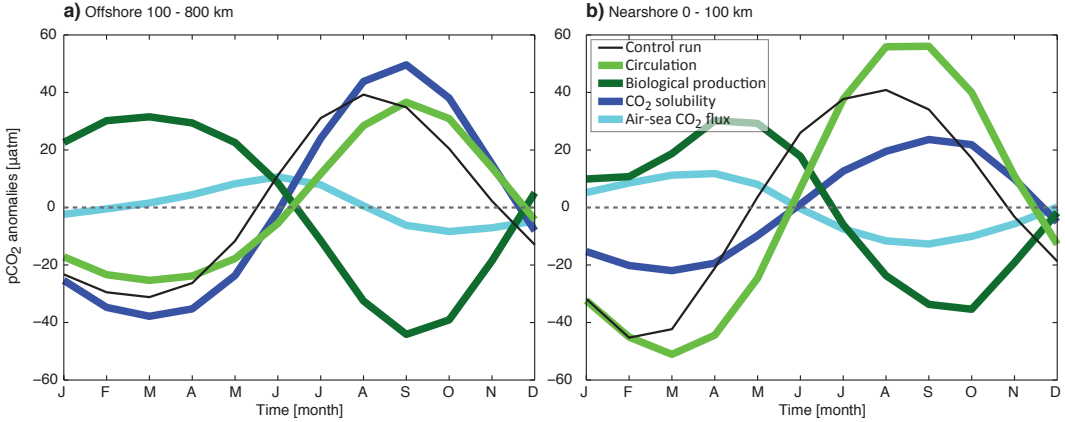

Fig. 10. Monthly mean pCO_2 anomalies for the offshore **(a)** and the nearshore **(b)** domains: the colored lines represent the contributions of ocean circulation, biological production, CO_2 solubility and air–sea CO_2 flux to monthly mean pCO_2 anomalies from the control simulation (black line).

BGD
10, 14043–14091, 2013

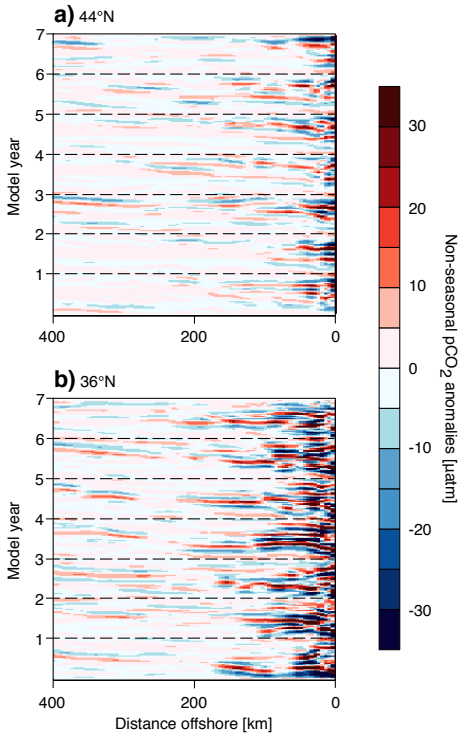

Fig. 11. Hovmöller diagrams (Hovmöller, 1949) representing non-seasonal pCO_2 anomalies as a function of distance offshore, based on 2-day output spanning seven consecutive model years. The anomalies were computed as the difference between the total pCO_2 over the seven analysis years and a seasonal fitted mean over the same seven years, and were smoothed with 40-day running mean. Panel **(a)** shows a transect at around 44° N, while panel **(b)** depicts a transect at around 36° N. The transects run roughly along the midlines of the northern and central subdomains, respectively. We do not show any transects for the southern subdomain, as any activity attributable to mesoscale eddies was negligible compared to the other two subdomains.

BGD
10, 14043–14091, 2013